Sgr A∗ X-ray flares from non-thermal particle acceleration in a magnetically arrested disc

Nicolas Scepi [1]∗ Jason Dexter [1,2] and Mitchell C. Begelman[1,2]

[1] *JILA, University of Colorado and National Institute of Standards and Technology, 440 UCB, Boulder, CO 80309-0440, USA*
[2] *Department of Astrophysial and Planetary Sciences, University of Colorado, 391 UCB, Boulder, CO 80309-0391, USA*

ABSTRACT

Sgr A∗ exhibits flares in the near-infrared and X-ray bands, with the luminosity in these bands increasing by factors of 10–100 for ≈60 min. One of the models proposed to explain these flares is synchrotron emission of non-thermal particles accelerated by magnetic reconnection events in the accretion flow. We use the results from particle-in-cell simulations of magnetic reconnection to post-process 3D two-temperature GRMHD simulations of a magnetically arrested disc (MAD). We identify current sheets, retrieve their properties, estimate their potential to accelerate non-thermal particles, and compute the expected non-thermal synchrotron emission. We find that the flux eruptions of MADs can provide suitable conditions for accelerating non-thermal particles to energies $\gamma_e \lesssim 10^6$ and producing simultaneous X-ray and near-infrared flares. For a suitable choice of current-sheet parameters and a simplified synchrotron cooling prescription, the model can simultaneously reproduce the quiescent and flaring X-ray luminosities as well as the X-ray spectral shape. While the near-infrared flares are mainly due to an increase in the temperature near the black hole during the MAD flux eruptions, the X-ray emission comes from narrow current sheets bordering highly magnetized, low-density regions near the black hole, and equatorial current sheets where the flux on the black hole reconnects. As a result, not all infrared flares are accompanied by X-ray ones. The non-thermal flaring emission can extend to very hard ($\lesssim$ 100 keV) X-ray energies.

Key words: acceleration of particles – accretion, accretion discs – magnetic field – radiation mechanisms: non-thermal – Galaxy: centre.

1 INTRODUCTION

First discovered in the radio (Balick & Brown 1974), the supermassive black hole at the centre of our Galaxy, Sagittarius A∗ (Sgr A∗), is now routinely observed in the near-infrared (NIR; Genzel et al. 2003), X-ray (Baganoff et al. 2001), and gamma-ray bands (Mayer-Hasselwander et al. 1998). It is now accepted that the emission from Sgr A∗ comes from an optically thin, hot accretion flow around a black hole of mass 4×10^6 M$_\odot$ (Ghez et al. 2005; Gillessen et al. 2017; Gravity Collaboration 2018a). With a bolometric luminosity of $\approx 5 \times 10^{35}$ erg s^{-1} (Bower et al. 2019), Sgr A∗ is accreting at a very sub-Eddington rate and is the best laboratory to study radiatively inefficient accretion flows (Yuan & Narayan 2014).

In its quiescent state, the spectrum of Sgr A∗ typically extends from radio to NIR wavelengths and is thought to originate from synchrotron emission of a population of relativistic, thermal electrons in a magnetic field of ≈100 G (Bower et al. 2019). In quiescence, the level of X-rays is lower than any other low-luminosity AGN and is believed to originate from thermal bremsstrahlung emission near the Bondi radius (Quataert 2002; Baganoff et al. 2003).

Several times a day, Sgr A∗ shows events of strong variability in the NIR and X-ray bands, called flares (Baganoff et al. 2001; Genzel et al. 2003; Ghez et al. 2005; Neilsen et al. 2013). During a flare the luminosity in the X-rays and in the NIR can rise by a factor as large as ≈100 (Do et al. 2019; Haggard et al. 2019). Since the sub-millimeter emission does not show simultaneous, large-amplitude variability (e.g. Eckart et al. 2006a; Marrone et al. 2008; Yusef-Zadeh et al. 2008), it is usually assumed that these events are due to a separate, possibly non-thermal, population of electrons (Markoff et al. 2001). Given that the NIR emission is highly polarized (Eckart et al. 2006b), it is further assumed that these electrons radiate their energy via synchrotron emission (Dodds-Eden et al. 2009; Ponti et al. 2017), although a synchrotron self-Compton origin for the X-rays may also be possible (e.g. Eckart et al. 2012; Dibi et al. 2016).

Recently, the GRAVITY instrument was able to resolve the motion of the NIR centroid during a flaring event, showing a clockwise, continuous rotation consistent with a region of emission located at a few gravitational radii, r_g, from the central black hole (Gravity Collaboration 2018b). This result suggests that the particles responsible for the flaring are accelerated in a compact, rotating region near the black hole.

One scenario to produce these features is the presence of magnetic reconnection events in a collisionless, hot plasma rotating around the black hole. The magnetic reconnection scenario is supported by the results of particle-in-cell (PIC) simulations showing that the parallel electric field generated during reconnection events can accelerate particles to very high energies, producing a power-law distribution of electrons with hard indices (Bessho & Bhattacharjee 2012; Cerutti et al. 2012, 2013; Kagan, Milosavljević & Spitkovsky 2013; Guo

∗ E-mail: nicolas.scepi@gmail.com

et al. 2014; Sironi & Spitkovsky 2014; Guo et al. 2016; Werner et al. 2016, 2018; Werner, Philippov & Uzdensky 2019). Synchrotron emission from a non-thermal distribution of electrons of index ≈ 2 could explain the flaring spectrum of Sgr A∗ (Dodds-Eden et al. 2009).

Although PIC simulations are able to resolve the plasmoid dynamics and the subsequent particle acceleration, they are restricted to very limited computational domains. Current sheets are apparent at all times in general relativistic magnetohydrodynamic (GRMHD) simulations (e.g. Gammie, McKinney & Tóth 2003; Hirose et al. 2004). When using explicit resistivity, they reconnect into plasmoids (Ripperda, Bacchini & Philippov 2020), and may provide potential locations for magnetic reconnection flares. However, the details of non-thermal particle acceleration require a kinetic approach, such as that provided by PIC.

Nevertheless, much effort has been put into modeling Sgr A∗ from first-principles GRMHD simulations. For the low Eddington ratio of Sgr A∗, radiative cooling can be safely neglected (Dibi et al. 2012; Ryan et al. 2017) and observables can be calculated in post-processing. Since the plasma is collisionless, electrons and ions are not necessarily thermally coupled. Radiative transfer calculations must either assign an ion to electron temperature ratio (e.g. Mościbrodzka et al. 2009; Dexter et al. 2010; Shcherbakov, Penna & McKinney 2012; Chan et al. 2015b) or evolve the electron entropy separately (Ressler et al. 2015; Ryan et al. 2017; Chael et al. 2018; Dexter et al. 2020a). In the latter case, the total heating rate is divided into electrons and ions using some sub-grid prescription based on kinetics calculations (Howes 2010; Rowan, Sironi & Narayan 2017; Werner et al. 2018; Kawazura, Barnes & Schekochihin 2019). In almost all cases, the electron distribution function has been assumed to be purely thermal.

Radiative models from GRMHD simulations can generically reproduce the shape of the Sgr A∗ spectral peak in the sub-millimeter and its compact source size (Doeleman et al. 2008). Turbulence driven by the magnetorotational instability (Balbus & Hawley 1991; Balbus & Hawley 1998) can also explain the $\simeq 30$ per cent sub-mm flux density fluctuations (Dexter, Agol & Fragile 2009). Current GRMHD models have more difficulty in reproducing the large-amplitude NIR and X-ray flares. In the NIR, promising scenarios include misaligned accretion discs (Dexter & Fragile 2013; White & Quataert 2021), gravitational lensing events (Chan et al. 2015a), electron heating at the jet wall near the event horizon (e.g. Ressler et al. 2017), and magnetic eruptions in strongly magnetized discs (Dexter et al. 2020b; Porth et al. 2021). Efforts to introduce non-thermal electrons to model flares (e.g. Ball et al. 2016; Chatterjee et al. 2020; Petersen & Gammie 2020) show some promise. However, so far they have difficulty reproducing the large contrast in X-ray luminosity between flares and quiescence, and the lack of corresponding increases in the sub-millimeter luminosity.

Magnetically arrested discs (MAD; Bisnovatyi-Kogan & Ruzmaikin 1974) are characterized by stochastic eruption events of magnetic flux from near the black hole (e.g. Igumenshchev 2008; Tchekhovskoy, Narayan & McKinney 2011). Dexter et al. (2020b) found that GRMHD models of MADs with self-consistent electron heating provide a promising scenario for explaining Sgr A∗ flares. The infrared flare luminosity, time-scale, and recurrence time from magnetic flux eruptions near the black hole are broadly consistent with those observed. Electron heating in rotating interfaces between magnetically dominated bubbles and high density gas caused rotating flaring emission regions, whose photocentre and linear polarization evolution seem promisingly similar to those found in GRAVITY

observations (Gravity Collaboration 2018b; Gravity Collaboration 2020a, c). In these simulations, energy disspation occurs from (numerical) magnetic reconnection, and the current sheets involved seem promising for accelerating particles to high energy (Porth et al. 2021). However, that work assumed a purely thermal electron distribution.

Here, we assess the potential of magnetic eruption events in MADs for producing luminous X-ray flares due to synchrotron radiation from a non-thermal distribution of electrons accelerated by magnetic reconnection. In Section 2, we introduce our methods for identifying reconnecting current sheets in ideal GRMHD, retrieving their properties, and estimating their potential for accelerating non-thermal particles. We calculate approximate spectra and light curves from the resulting non-thermal distribution function in Section 3, and show that luminous X-ray flares are likely to result from eruption events. For some parameter choices, the resulting quiescent and flaring luminosities match those observed from Sgr A∗. In Section 4, we discuss the implications of our results and directions for future work.

2 METHODS

In this section we describe our method to identify current sheets, to retrieve the properties of these current sheets, to assign a non-thermal particle distribution at each cell, and to estimate the subsequent synchrotron emission coming from each cell.

2.1 Numerical set-up

We use the results of a 3D MAD GRMHD simulation and a standard accretion and normal evolution (SANE) GRMHD simulation, both already presented in Dexter et al. (2020a). We will present the general properties of the simulations but for more information the reader can refer to Dexter et al. (2020a). The GRMHD simulations were performed with the public code HARMPI[1] (Tchekhovskoy 2019) that includes a scheme to evolve electron internal energy densities along with that of the MHD fluid (Ressler et al. 2015). We use an adiabatic equation of state with a relativistic adibatic index of 4/3 for the electrons and a non-relativistic adiabatic index of 5/3 for the MHD fluid. The prescription for electron heating that is used for the MAD and SANE simulation derives from the PIC reconnection study of Werner et al. (2018).

The simulations were initialized from a Fishbone–Moncrief torus (Fishbone & Moncrief 1976) with an inner radius of 12 r_g, pressure maximum at 25 r_g, and a black hole spin parameter of $a = 0.9375$. The simulation grid uses coordinates based on a spherical-polar Kerr–Schild metric, which are distorted in the θ-direction in order to better resolve the equatorial inner accretion flow and extended relativistic jet. The radial coordinate is logarithmically spaced. The grid resolution is $320 \times 256 \times 160$ in the r, θ, and ϕ directions, respectively. The magnetic field configuration is initialized as a single poloidal field loop, whose amplitude is chosen so that $\max(p_g)/\max(p_B) = 100$, where p_g is the gas pressure and $p_B \equiv b^\mu b_\mu/2$ the magnetic pressure and whose radial profile is chosen so as to produce either a MAD or a SANE.

The MAD simulation has been run for $9 \times 10^4\, r_g/c$ and has established an inflow equilibrium up to $\approx 90\, r_g$ by the end of the simulation. The simulation becomes MAD around $6 \times 10^3\, r_g/c$. The

---

[1] https://github.com/atchekho/harmpi

SANE simulation has been run for $19 \times 10^4 \, r_g/c$ so that it also achieves an inflow equilibrium up to $\approx 90 \, r_g$.

2.2 Identification of current sheets

In ideal MHD, the electromagnetic field tensor can be expressed as

$$F^{\mu\nu} = \epsilon^{\mu\nu\kappa\lambda} u_\kappa b_\lambda, \tag{1}$$

where u_μ is the covariant four-velocity, b_μ is the covariant four-magnetic field, $\epsilon^{\mu\nu\kappa\lambda} = (-1/\sqrt{-g})[\mu\nu\kappa\lambda]$, with $[\mu\nu\kappa\lambda]$ the completely antisymmetric symbol and $g = \det(g_{\mu\nu})$ (Gammie et al. 2003). The four-current is expressed as

$$\mathcal{J}^\mu = F^{\mu\nu}_{\;\;;\nu}, \tag{2}$$

where $_{;\mu}$ represents the covariant derivative. Using the symmetry of the Christoffel symbol about its lower indices and the anti-symmetry of the electromagnetic field tensor gives

$$\mathcal{J}^\mu = \frac{1}{\sqrt{-g}} \partial_\nu(\sqrt{-g} F^{\mu\nu}). \tag{3}$$

To obtain a reasonable estimate of the current without taking approximate time derivatives from our data, we transform the electromagnetic tensor to the rest frame of the fluid where the electric current vanishes. We then approximate the derivatives in the rest frame with derivatives in the coordinate frame to approximate the current in the rest frame as

$$\bar{\mathcal{J}}^i \approx \frac{1}{\sqrt{-g}} \partial_j(\sqrt{-g} \bar{F}^{ij}), \tag{4}$$

where barred quantities are computed in the rest frame. We verified on one snapshot that computing the current from equation (3) on the fly in our simulation only leads to a 20 per cent difference in the norm of the current compared to the approximate value from equation (4). We then introduce the parameter

$$\mathcal{C} \equiv \frac{|\bar{\mathcal{J}}|\delta}{|b|}, \tag{5}$$

where $|\bar{\mathcal{J}}| = \sqrt{\bar{\mathcal{J}}^\mu \bar{\mathcal{J}}_\mu}$, $|b| = \sqrt{b^\mu b_\mu}$ and δ is the size of a cell in the rest frame (Bodo, Tavecchio & Sironi 2021). Since high values of $\mathcal{C}$ correspond to zones of high current and low magnetic field, we use this parameter to identify potentially reconnecting current sheets in our simulations. Bodo et al. (2021) verified that the current sheets found with this method are very similar to those found with the more advanced algorithm developed in Zhdankin et al. (2013).

Figs 1 and 2 show equatorial (left) and poloidal (two right) cuts of $\mathcal{C}$ where we used different thresholds, $\mathcal{C}_{\min} = 0.3$, 1 or 3, during and outside a magnetic eruption event. In both cases, we identify thin elongated structures that resemble current sheets. The lower the threshold $\mathcal{C}$, the thicker and the more numerous become the current sheets. Our method identifies similar patterns of current sheets during and outside eruption events. However, as we will see in Section 3.1, the current sheet properties are very different in these two cases.

2.3 Properties of the current sheets and non-thermal particle distribution

To assess the potential of the currents sheets as non-thermal particle accelerators, we need to systematically retrieve their physical properties. Important quantities in reconnection studies are the upstream cold magnetization, $\sigma_{\rm up} = b^2/\rho$, and the upstream plasma β-parameter, $\beta_{\rm up}$, as well as the local number density of electrons, n_e, the local electron temperature, T_e, and the local magnetic field
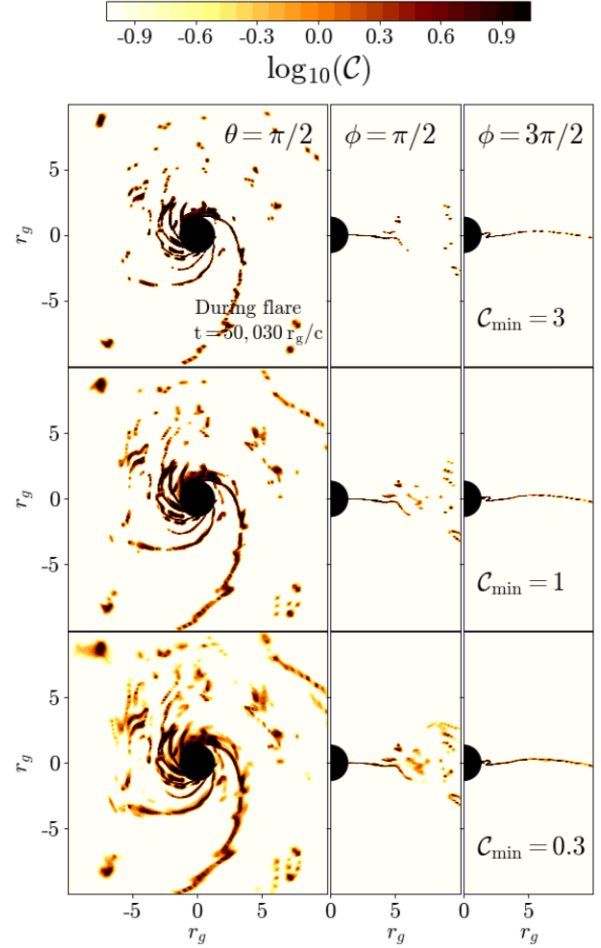
Figure 1. Selection of current sheets during a flaring event at $t = 50,030 \, r_g/c$. Current sheets are found both during and outside flares. From left to right: Equatorial cut at $\theta = \pi/2$ and poloidal cuts at $\phi = \pi/2$ and $\phi = 3\pi/2$. From top to bottom, we used $\mathcal{C}_{\min} = 3$, 1 and 0.3.

strength, B (Werner et al. 2018). We define the local properties as the properties of a given cell in our GRMHD simulation and the upstream properties as the properties of the surrounding cells. To retrieve the upstream properties we draw a sphere of five cells[2] around each cell and look for the most magnetized cell, which we then assume to give the magnetization of the upstream region.

We then use the upstream properties and local properties of the current sheets to assign to each cell a modified electron κ-distribution. The κ-distribution is a hybrid distribution composed of a thermal bulk of electrons at low energy and a non-thermal power-law tail at high energy, which is, in the relativistic regime, expressed as

$$\frac{dn_e}{d\gamma} = N\gamma(\gamma^2 - 1)^{1/2} \left(1 + \frac{\gamma - 1}{\kappa w}\right)^{-(\kappa+1)} \times e^{-\gamma/\gamma_{\rm cut}}. \tag{6}$$

Our modification consists of an exponential cutoff at high energies, $\gamma_{\rm cut}$, the value of which depends on cooling as explained in Sec-

---

[2]Our choice of five cells is the minimum number of cells required to produce enough hard non-thermal power-law emission. For less than five cells the emission becomes steeper due to the low magnetic field inside the current sheets. For more than five cells the non-thermal emission does not change much with an X-ray flux that is only two times higher for 20 cells than for five cells at $t = 50,300 \, r_g/c$ and for $\mathcal{C}_{\min} = 1$.
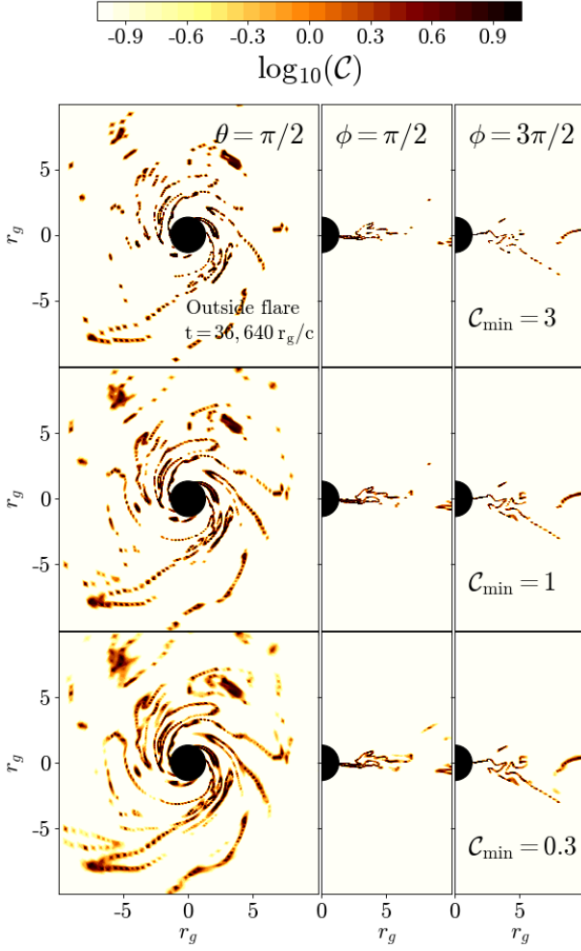
Figure 2. Selection of current sheets during a non-flaring epoch at $t = 36,640$ r_g/c. We see similar patterns of current sheets in both the flaring and non-flaring cases. From left to right: Equatorial cut at $\theta = \pi/2$ and poloidal cuts at $\phi = \pi/2$ and $\phi = 3\pi/2$. From top to bottom, we used $\mathcal{C}_{\min} = 3$, 1 and 0.3.

tion 2.5. Here, n_e is the number density of electrons, γ is the Lorentz factor, N is a normalization factor, $\kappa = p + 1$, p is the index of the power-law tail, γ^{-p}, and w is a parameter defining the width of the distribution, which tends to θ_e, the dimensionless electron temperature $k_B T_e/m_e c^2$, as the power-law component becomes very steep.

Using the results of PIC simulations, we can constrain the value of p from the upstream and local properties of the current sheets. We use the following scaling law from Ball, Sironi & Özel (2018) and Werner et al. (2018):

$$p = A_p + B_p \tanh(C_p \beta_{\mathrm{up}}), \tag{7}$$

where $A_p = 1.8 + 0.7/\sqrt{\sigma_{\mathrm{up}}}$, $B_p = 3.7\sigma_{\mathrm{up}}^{-0.19}$, $C_p = 23.4\sigma_{\mathrm{up}}^{0.26}$.

Once we constrain the power-law index of the κ-distribution, we need to constrain the two remaining parameters that are the normalization factor N and the width of the distribution w. To do that, we use the two first moments of the electron energy distribution,

$$n_e = \int_1^\infty \frac{\mathrm{d}n_e}{\mathrm{d}\gamma} \mathrm{d}\gamma, \tag{8}$$

$$u_e = \int_1^\infty \gamma \frac{\mathrm{d}n_e}{\mathrm{d}\gamma} \mathrm{d}\gamma, \tag{9}$$

where $n_e = n_i = \rho/m_p$ from the fluid mass density and u_e is the self-consistently evolved electron internal energy density.

2.4 Synchrotron emission

We estimate the synchrotron emission of a thermal and a κ-distribution of electrons by using the fitting formulæ of Pandya et al. (2016). The synchrotron emissivity in vacuum can be written as

$$j_S = \frac{n_e e^2 \nu_c}{c} J_S\left(\frac{\nu}{\nu_c}, \theta\right), \tag{10}$$

where the formula for J_S depends on the electron distribution, $\nu_c \equiv e|b|/(2\pi m_e c)$ is the electron cyclotron frequency, and θ is the angle between the observer and the magnetic field.

For a relativistic thermal distribution, Pandya et al. (2016) find

$$J_S = \frac{\sqrt{2}\pi}{27} e^{-X^{1/3}} \sin(\theta)(X^{1/2} + 2^{11/12}X^{1/6})^2, \tag{11}$$

where $X \equiv \nu/\nu_s$ and $\nu_s \equiv (2/9)\nu_c \theta_e^2 \sin(\theta)$.

For a κ-distribution, they find

$$J_S = (J_{S,\mathrm{low}}^{-x} + J_{S,\mathrm{high}}^{-x})^{-1/x}, \tag{12}$$

where

$$J_{S,\mathrm{low}} = X_\kappa^{1/3} \sin(\theta) \frac{4\pi \Gamma(\kappa - 4/3)}{3^{7/3}\Gamma(\kappa - 2)} \tag{13}$$

$$J_{S,\mathrm{high}} = X_\kappa^{-(\kappa-2)/2} \sin(\theta) 3^{(\kappa-1)/2} \frac{(\kappa - 2)(\kappa - 1)}{4}$$

$$\times \Gamma\left(\frac{\kappa}{4} - \frac{1}{3}\right) \Gamma\left(\frac{\kappa}{4} + \frac{4}{3}\right), \tag{14}$$

$X_\kappa \equiv \nu/\nu_\kappa$, $\nu_\kappa \equiv \nu_c(w\kappa)^2$, $x = 3\kappa^{-3/2}$, and Γ is the gamma function.

Once we have computed the emissivities, we compute the thermal absorptivity, $\alpha_S \equiv j_S/B_\nu$, where $B_\nu \equiv (2h\nu^3/c^2)[\exp(h\nu/kT_e) - 1]^{-1}$ is the Planck function.[3] We then integrate the radiative transfer equation along the θ-coordinate[4] to compute the luminosity,

$$L_\nu = \int_{\mathrm{ergo}}^{50r_g} \int_0^{\tau_\nu} \int_0^{2\pi} e^{-(\tau_\nu(r,\pi,\phi) - \tau_\nu(r,\theta,\phi))}$$

$$\times j_S \times g_{\mathrm{redshift}}^3 \sqrt{-g} \mathrm{d}r \mathrm{d}\theta \mathrm{d}\phi. \tag{15}$$

where $\tau_\nu \equiv \int_0^\theta \alpha_S \mathrm{d}s$ is the local total optical depth in the disc along θ, $\mathrm{d}s = \sqrt{g_{\theta\theta}}\mathrm{d}\theta$, $g_{\mathrm{redshift}} \equiv \sqrt{A\Sigma/\Delta}$ is the gravitational redshift between the emitted frequency in the rest-frame and the frequency received by a distant static observer (Viergutz 1993) with $A = (r^2 + a^2)^2 - a^2\Delta\sin^2\theta$, $\Sigma = r^2 + a^2\cos^2\theta$, and $\Delta = r^2 - 2rM + a^2$ and M, the mass of the central object, is set to 1 in this formula. In order to further take into account the gravitational effects, we also remove all the emission coming from the ergosphere since the redshift effects are usually large in this region, making it very dim. Note that, as in (Dexter et al. 2020a), we ignore the emission coming from the regions where $\sigma > 1$ since these regions are likely to be affected by numerical floors.

This simple integration allows us to take into account the synchrotron self-absorption (this is only important at low frequencies since the plasma is optically thin at frequencies higher than $\approx 10^{12}$ Hz) as well as part of the general relativistic effects. The approximation

---

[3] We use the Kirchoff's law to compute the absorptivity since non-thermal electron emission is only important at high frequencies where the plasma is optically thin.

[4] Since most of the emission comes from the bulk of the disc, integrating along θ is almost equivalent to integrating along straight vertical lines.

is most suitable for low inclination angle (almost face-on), since we neglect Doppler beaming and gravitational lensing effects. We show below that the induced errors in the flared thermal NIR emission, although it originates from very close to the black hole where gravitational effects are important, are of order unity, while here we are mainly interested in order-of-magnitude estimates of the flaring and quiescent non-thermal X-ray luminosity.

2.5 Effect of cooling on the particle distribution

Cooling can affect the particle distribution in two ways. Very strong cooling can prevent the acceleration of high energy particles in the reconnecting current sheet in the first place. This happens if the synchrotron cooling time-scale is shorter than the acceleration time-scale due to the non-ideal electric field in the current sheet. The time-scales are equal for an electron Lorentz factor $\gamma_{\rm rad} \equiv \sqrt{3 e E_{\rm rec}/(4\sigma_{\rm T} U_{\rm B})}$ where $E_{\rm rec} \approx 0.1|b|$ is the non-ideal electric field (Uzdensky, Cerutti & Begelman 2011), e is the electron charge, $\sigma_{\rm T}$ is the Thomson cross-section, and U_B is the magnetic energy density. Based on the strong inverse-Compton cooling PIC simulations by Werner et al. (2019), we use a precription for the cutoff frequency at each cell that depends on the value of $\gamma_{\rm rad}$,

$$\gamma_{\rm cut} = \frac{\gamma_{\rm rad}}{\sqrt{1 + 0.0625(\gamma_{\rm rad}/(m_p/m_e)\sigma_{\rm up})^2}}. \tag{16}$$

When cooling is weak, $\gamma_{\rm cut} = 4(m_p/m_e)\sigma_{\rm up}$ (Werner et al. 2016). When cooling is strong, $\gamma_{\rm cut} = \gamma_{\rm rad}$. We find that we never actually reach the strong cooling regime and that the cutoff is located at $\approx 4(m_p/m_e)\sigma_{\rm up}$. Note that our choice of $\gamma_{\rm cut}$ for weak cooling is rather conservative since PIC simulations show that particles can be accelerated to higher energies in plasmoids at later times, with the cutoff frequency going as the square root of time (Petropoulou & Sironi 2018; Hakobyan et al. 2021).

The second way that cooling can affect the particle distribution is by cooling the particles after they have been accelerated. In particular, it is well-known that if particles do not have time to cool before they get advected on to the black hole or leave the system (weak cooling), then the particle distribution is similar to the spectrum of injected particles. However, if particles can cool before they leave the system (strong cooling), the power-law index of the particle distribution is steepened by 1 compared to the weak cooling case (Blumenthal & Gould 1970). To assess whether the cooling can significantly affect the particle distribution or not we compare the synchrotron cooling time, $t_{\rm synch}$,

$$t_{\rm synch} = \frac{3 m_e c}{4 \sigma_T U_B \gamma \beta^2}, \tag{17}$$

to the escape time-scale that we take to be of the order of the light crossing time

$$t_{\rm esc} = \frac{r_g}{c}. \tag{18}$$

If we assume that $\beta \equiv v/c \approx 1$, which can be verified to be a good approximation *a posteriori*, we find that the cooling becomes significant around

$$\gamma_{\rm break} \approx 3.9 \times 10^3 \left(\frac{|b|}{100\,G}\right)^{-2} \tag{19}$$

which gives a typical break frequency of

$$\nu_{\rm break} \approx 2.5 \times 10^{15} \left(\frac{|b|}{100\,G}\right)^{-1}\,{\rm Hz}, \tag{20}$$

so that the cooling break should be located somewhere in the UV. For $\gamma > \gamma_{\rm break}$ we then steepen the power-law index of the particle distribution function from p to $p + 1$ and the spectral index of the synchrotron emissivity in each cell by 1/2, from $(p - 1)/2$ to $p/2$. In practice, we divide equation (12) by $\sqrt{\nu/\nu_{\rm break}}$ when $\nu > \nu_{\rm break}$, where $\nu_{\rm break}$ is the synchrotron frequency for an electron with a Lorentz factor $\gamma_{\rm break}$. Note that $\gamma_{\rm break}$ is a local property of each cell.

We also tried to approximate the escape time-scale with the accretion time-scale, $r \times u^t/u^r \approx 100\,r_g/c$. However, in this case all the particles with $\gamma \gtrsim 10$ have enough time to cool and the power-law break is in the sub-millimeter. This would drastically reduce the emission in the X-rays. Note that a short escape time-scale, comparable to the dynamical time-scale is empirically supported by the short duration of the flares (<1h) in Sgr A*.

3 RESULTS

In this section we present the results of our analysis, starting in Section 3.1 with the current sheets properties, followed by the emitted spectrum in Section 3.2 and the emitted light curves in Section 3.3. In Section 3.4 we carry out the same analysis on a SANE simulation, and compare the results with the MAD case.

3.1 Emission properties of the current sheets

Figs 1 and 2 show the current sheets that are selected by our method (see Section 2.2) in a MAD simulation at two different moments, corresponding to a magnetic flux eruption during which a large, magnetized bubble is expelling the flux from the black hole (Fig. 1), and during a relatively quiescent period showing no eruptions (Fig. 2). The first striking result to note is that our method selects a similar number of current sheets regardless of whether an eruption event is underway.

By comparing the bottom panels of Figs 3 and 4, however, which show the X-ray luminosity at 10^{18} Hz, we see that the emission properties of the current sheets during and outside the magnetic eruption are very different. This is mostly due to the fact that during an eruption, the current sheets are surrounded by regions of high magnetization while outside an eruption the current sheets are surrounded by regions of low magnetization.

We can see from the poloidal cut at $\phi = 3\pi/2$ on Figs 1 and 3 that during a magnetic eruption there is a strong current sheet forming in the region evacuated by the low-density bubble that is surrounded by material with $\sigma_{\rm up} \approx 100$. In the same way, we can see from the equatorial cut at $\theta = \pi/2$ that the equatorial current sheet forming in the bubble is also surrounded by material with $\sigma_{\rm up} \approx 100$. Thanks to their high upstream magnetization, these current sheets have the properties required to lead to efficient non-thermal particle acceleration and so produce significant X-ray emission.

Contrary to the conditions during a magnetic flux eruption, a comparison between Figs 2 and 4 shows that the current sheets forming in the absence of a magnetic flux eruption are surrounded by regions of much lower magnetization. This leads to very weak non-thermal particle acceleration and little X-ray emission.
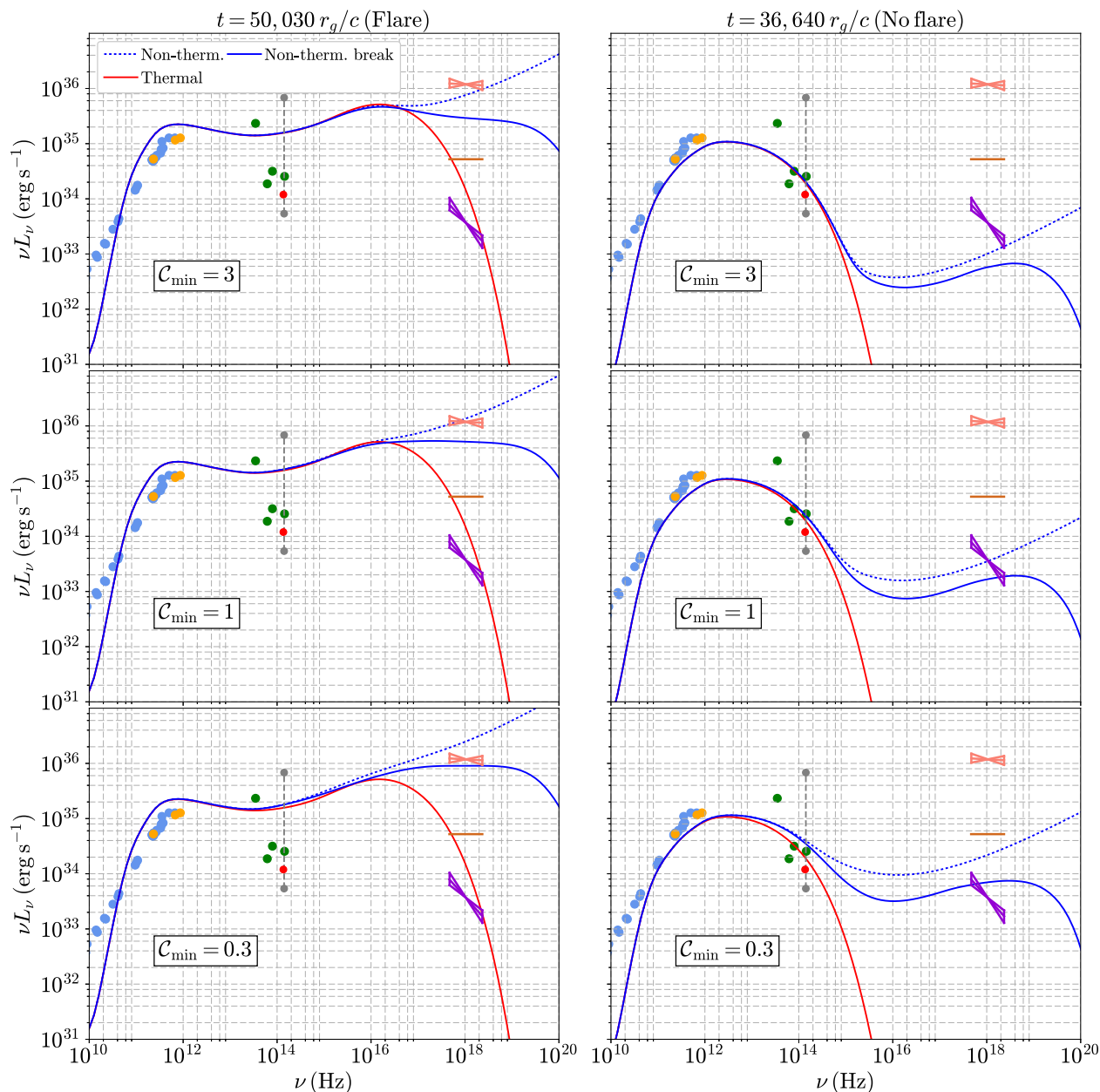
3.2 Spectra

Fig. 5 shows two sets of spectra obtained during a magnetic eruption and during a period with no magnetic eruptions, respectively, for three different values of $\mathcal{C}_{\rm min}$. For both cases the red line indicates the thermal synchrotron emission, the dotted blue line the non-thermal synchrotron emission ignoring the cutoff, and the solid
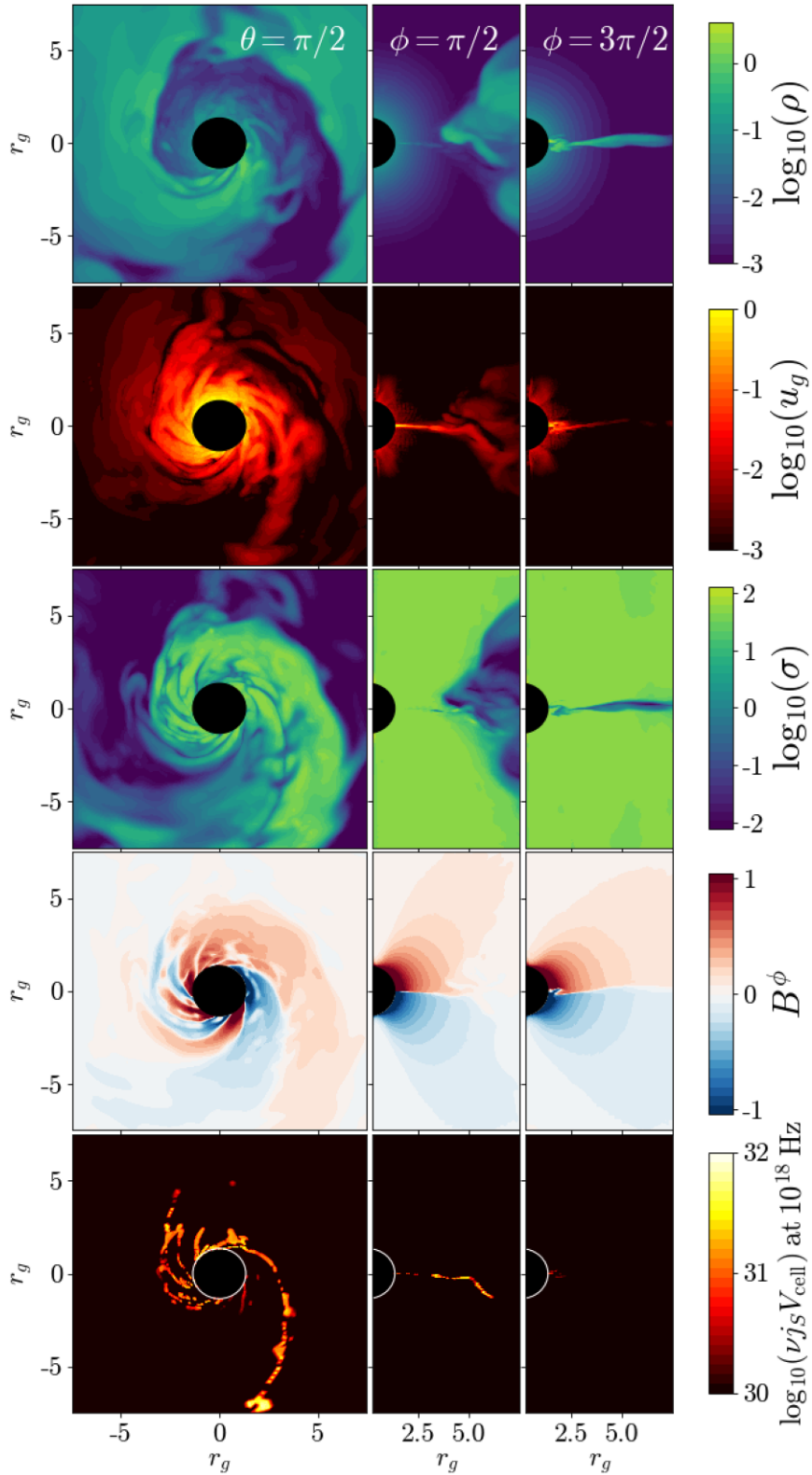
Figure 3. From top to bottom: Density in code units, internal energy in code units, rest mass magnetization, three-vector azimuthal magnetic field, and emitted spectral luminosity times frequency in the X-ray at 10^{18} Hz. From left to right: Cut in the midplane, cut at $\phi = \pi/2$, and cut at $\phi = 3\pi/2$. All images are made during a flare at $t = 50\,030\ r_g/c$.
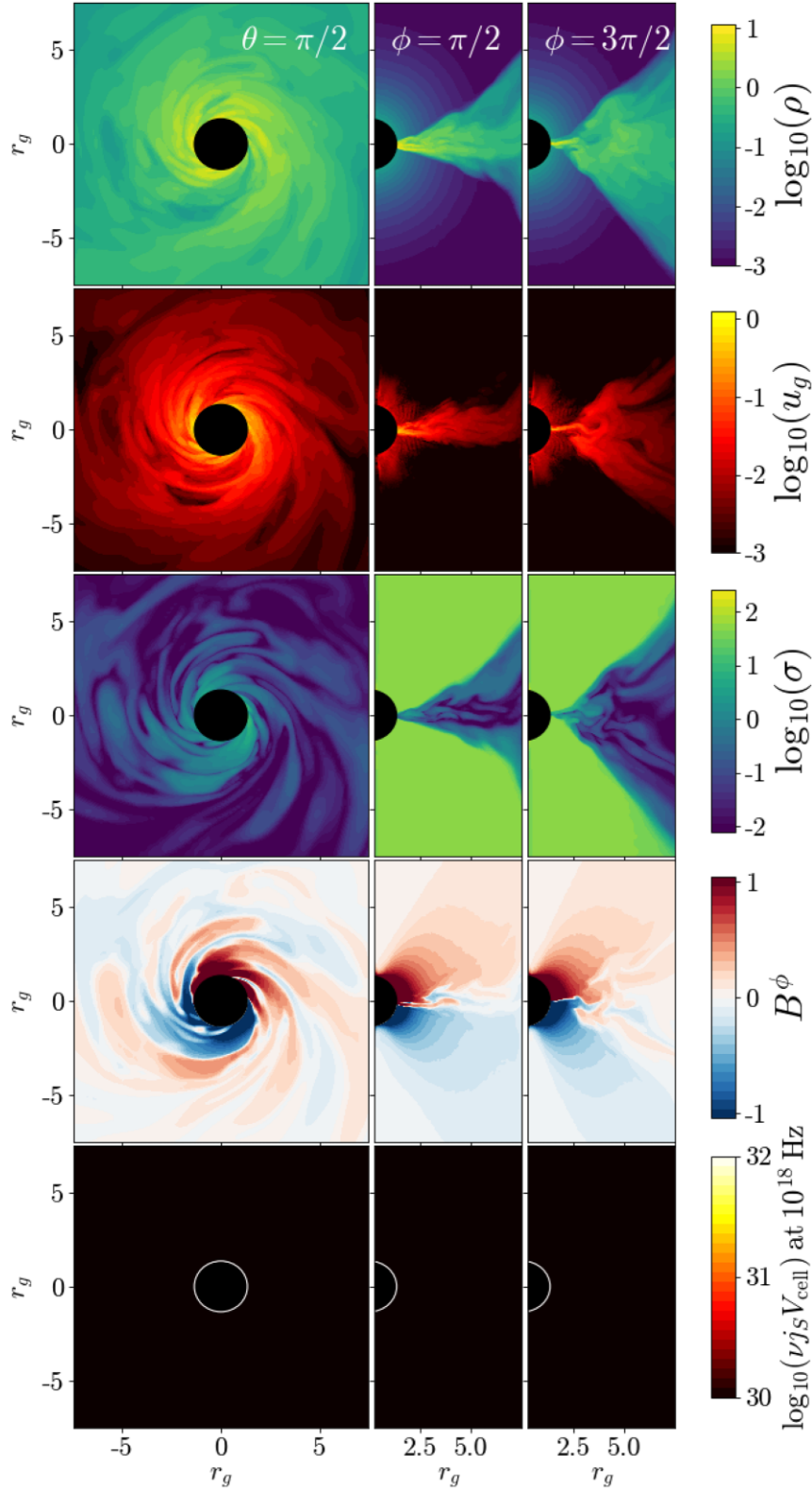
Figure 4. From top to bottom: Density in code units, internal energy in code units, rest mass magnetization, three-vector azimuthal magnetic field, and emitted spectral luminosity times frequency in the X-ray at 10^{18} Hz. From left to right: Cut in the midplane, cut at $\phi = \pi/2$, and cut at $\phi = 3\pi/2$. All images are made during a non-flaring epoch at t = 36 640 r_g/c.
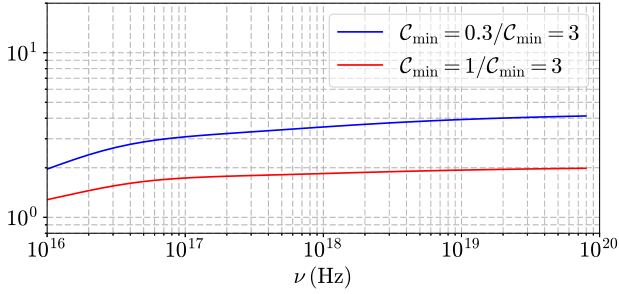
Figure 5. Spectra during a flare at $t = 50,030\, r_g/c$ (left-hand panels) and during a non-flaring epoch at t = 36 640 r_g/c (right-hand panels), for different threshold $\mathcal{C}_{\min} = 0.3$ (bottom), 1 (middle), and 3 (top). The red solid line indicates the thermal spectra, the dotted blue line the non-thermal spectra using a standard κ-distribution (without a high-energy cutoff and a cooling break), and the solid blue line the non-thermal spectra taking into account a cutoff in the particle distribution and a simple cooling break (see Section 2.5). We show the radio to sub-millimeter data points from the compilation of Connors et al. (2017) as light blue dots and the more recent data points from Bower et al. (2019) as orange dots. We also show the mid-infrared data points from Schödel et al. (2011) as green dots, the NIR maximum and minimum dereddened fluxes from Do et al. (2019) as grey circles, and the NIR median flux from Gravity Collaboration (2020b) as a red dot. Finally, we show the X-ray maximum flux ever detected by Haggard et al. (2019) and quiescent flux from Nowak et al. (2012) as a salmon and violet bowtie, respectively. We also show the mean flaring X-ray flux from Neilsen et al. (2015) as a chocolate line.

blue line the non-thermal synchrotron emission taking into account a cutoff in the particle distribution and a simple cooling break (see Section 2.5). For comparison, we show on Fig. 5 the data points from sub-millimeter to X-ray with the quiescent values as well as the maximum values ever observed at each frequency. To compare our model with the observations we normalize the flux at the sub-millimeter peak in the non-flaring case to the observed value.

Thermal synchrotron emission is always too weak to produce the observed luminosity of X-ray flares. During a magnetic eruption, the temperature rises because of energy dissipation in the reconnecting current sheets (Dexter et al. 2020a), provoking a thermal flare in the infrared, optical, UV, and up to the quiescent level of X-rays. Even for our most conservative value of $\mathcal{C}_{\min} = 3$, the non-thermal emission extends up to the X-rays at all times (left-hand and right-hand panels of Fig. 5). However, the non-thermal X-ray emission is always the

Figure 6. Ratio of the high energy non-thermal spectra found using $\mathcal{C}_{min} = 0.3$ and $\mathcal{C}_{min} = 3$ (blue) and $\mathcal{C}_{min} = 1$ and $\mathcal{C}_{min} = 3$ (red) during a flare at $t = 50\,030\ r_g/c$. This behaviour is also true outside of a flare although the ratio is larger than during a flare.

strongest during a magnetic flux eruption since the properties of the reconnecting current sheets are more favorable to efficient particle acceleration (see Section 3.1).

The luminosity at high energy increases strongly with decreasing $\mathcal{C}_{min}$ (Fig. 5). However, we can also see from the top panel of Fig. 6 that the shape of the spectrum at high energy does not really depend on our choice of $\mathcal{C}_{min}$. Indeed, the top panel of Fig. 6 shows that the ratio of the non-thermal emission in the X-rays for different values of $\mathcal{C}_{min}$ is almost a constant at high energies. This means that when we choose lower values of $\mathcal{C}_{min}$ we mostly increase the surface area of the reconnecting current sheets. This can be seen on Figs 1 and 2, where the effect of changing $\mathcal{C}_{min}$ is primarily to increase the length and width of the reconnecting current sheets. Note that the relative amplitude of flare to quiescent luminosity increases at higher $\mathcal{C}_{min}$.

For $\mathcal{C}_{min} = 1$ and 3 our model satisfactorily explains the spectra of Sgr A∗ during and outside of a flare. Indeed, for these two values

of $\mathcal{C}_{min}$ the NIR and X-ray emission almost reach the maximum values ever observed by Do et al. (2019) and Haggard et al. (2019), respectively, but also satisfy the quiescent levels of NIR and X-rays from Nowak et al. (2012) and Do et al. (2019). The relatively flat X-ray spectrum during the flare is also in good agreement with the observations from Haggard et al. (2019) and Neilsen et al. (2015). For $\mathcal{C}_{min} = 0.3$ the amount of X-rays in quiescence is too high to be consistent with observations.

3.3 Light curves

Fig. 7 shows a light curve in the NIR (bottom panel) and X-ray bands (middle panel) using $\mathcal{C}_{min} = 1$, as well as the normalized magnetic flux on the black hole (Tchekhovskoy et al. 2011). For the X-ray light curve, we choose to use $\mathcal{C}_{min} = 1$ since this value maximizes the amount of X-rays during a flare while providing a quiescent X-ray luminosity that remains marginally consistent (though slightly too high on average) with the observations (see Fig. 5). We note that our criterion of $\mathcal{C}_{min} = 1$ is also consistent with NIR flares and X-ray flares having roughly the same amplitude on average, in agreement with observations. We find that the flares in X-rays and NIR have a recurrence time of ≈10–20 h with amplitudes of ≈10 coincident with the flux eruptions, as found in Dexter et al. (2020b). Most of the time the X-ray and NIR flares are simultaneous, especially the biggest ones, however we do see some smaller NIR flares with a weak counterpart in X-rays, as can be seen on Fig. 7 at $t \approx 18$ or 72 h where indicated by the downward arrows. These NIR flares with a weak X-ray counterpart are due to current sheets that are not surrounded by a very magnetized medium. As we saw in Section 3.1, current sheets are forming all the time and converting magnetic energy into thermal energy to produce NIR flares but only those during magnetic flux eruptions have the required properties to create large simultaneous NIR and X-ray flares.
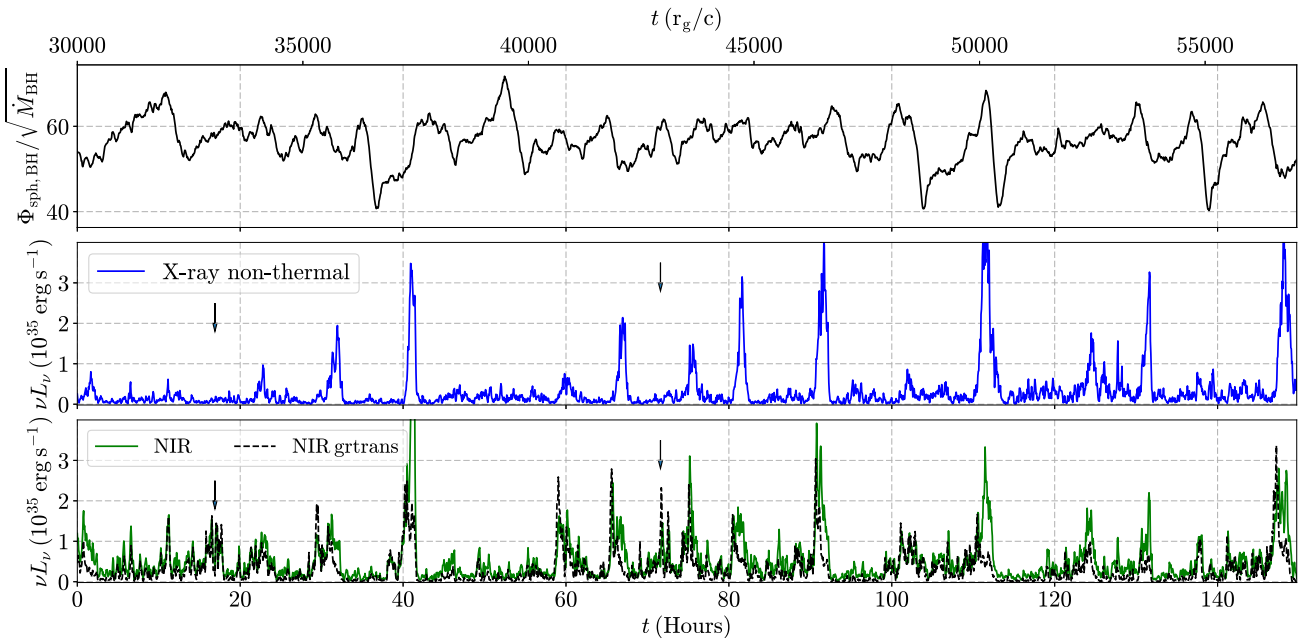
Figure 7. Top panel: Normalized magnetic flux on the black hole as a function of time. Middle panel: X-ray light curve at 10^{18} Hz with $\mathcal{C}_{min} = 1$. Bottom panel: NIR light curve at 10^{14} Hz with the contribution of non-thermal electrons (solid green line) with $\mathcal{C}_{min} = 1$, compared to a fully relativistic ray tracing calculation using only thermal electrons (dashed black line). The two downward arrows at $t \approx 18$ and 72 h indicate NIR flares that do not have an X-ray flaring counterpart.
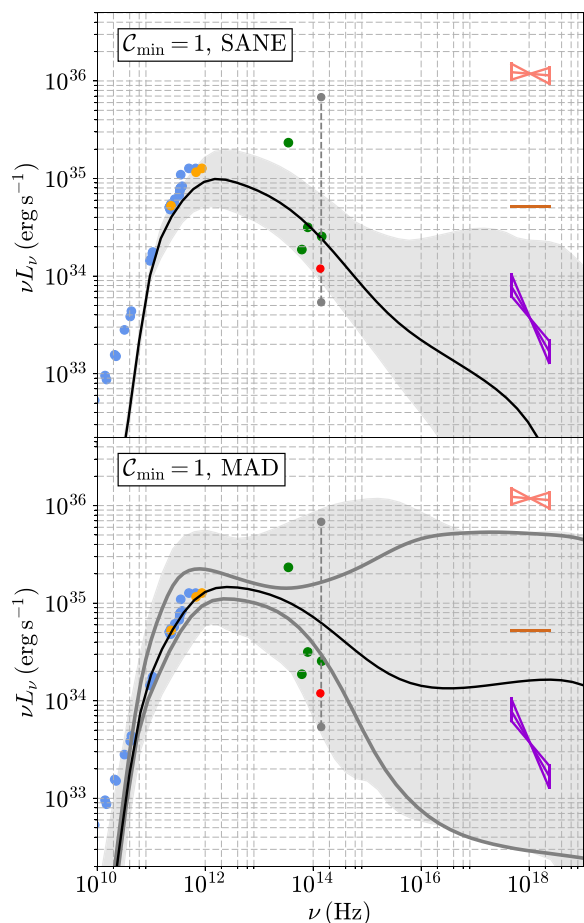
Figure 8. Comparison of spectra obtained from a SANE simulation (top) and a MAD simulation (bottom) for $\mathcal{C}_{\min} = 1$. The black solid line indicates the mean spectrum and the grey solid lines indicates the spectrum having the minimum and maximum X-ray luminosity at 10^{18} Hz. The grey shaded area indicates the range over which the entire spectrum varies and is computed by taking the minimum and maximum values at each frequency over time.

3.4 Comparison between MAD and SANE simulation

Fig. 8 shows a comparison of a MAD simulation (bottom panel) with a SANE simulation (top panel) with a value of $\mathcal{C}_{\min} = 1$ for both. The grey shaded regions shows the minimum and maximum values in time at all frequencies. The variability in the sub-millimeter and radio is slightly larger in the MAD than the SANE model. However, we see that compared to our MAD model, the SANE model emits very little at high frequencies above the UV. This difference is due to the absence of magnetic flux eruptions in the SANE model, which are necessary to produce strong, large-scale, highly magnetized reconnecting current sheets where a large amount of energy is dumped into thermal and non-thermal particles to create the NIR and X-ray flares. Even outside of the MAD flares, we find that the SANE model has lower emission at frequencies above $\approx 10^{15}$ Hz where the non-thermal emission dominates than our MAD model. This might be due to the overall higher magnetization of MAD discs compared to SANE discs, which favors non-thermal particle acceleration. Finally, we find that the mean spectra and variability obtained from our SANE simulation are in good agreement with the results of Chatterjee et al. (2020) and so confirm that SANE models are not

good candidates to explain the X-ray and NIR flaring behaviour of Sgr A∗.

4 DISCUSSION AND CONCLUSION

We have used GRMHD simulations of radiatively-inefficient black hole accretion flows to identify current sheets in a realistic geometry, retrieve their physical properties, estimate their potential for producing non-thermal high-energy particles, and compute the expected synchrotron emission in order to explain the X-ray flaring events in Sgr A∗. We have shown that in MADs, during magnetic flux eruptions, current sheets can form in highly magnetized regions heating the plasma but also producing non-thermal high energy particles with $\gamma \lesssim 10^6$. When post-processing the synchrotron emission of the disc, we find that the deposition of thermal energy during a magnetic eruption can power NIR flares while the deposition of energy in the non-thermal particles can power X-ray flares. The NIR and X-ray emission are inherently flaring since they are associated with magnetic flux eruption events that reccur on a time-scale of hours. Using a simplified synchrotron cooling prescription and a judicious choice of current sheet parameters (mainly a current-density threshold parameter $\mathcal{C}_{\min}$) we are able to reproduce, with a single set of parameters, the spectrum of Sgr A∗ in quiescence and in eruption from sub-millimeter to X-rays, with powerful X-ray flares reaching 5×10^{35} erg s^{-1}. This result is unique to MAD simulations and is not shared with SANE simulations, which show weak non-thermal particle acceleration and so produce little X-ray variability (Chatterjee et al. 2020).

One of the main caveats of our work is that we use ideal GRMHD simulations to identify reconnecting current sheets. The size and the dynamics of the current sheets is artificially governed by the finite resolution of our simulations. Hence, we cannot be certain in our quantification of the number of current sheets, their size or even the fact that they reconnect. Although the fundamental limit is the insufficient dynamic range of current global GRMHD simulations, a better quantification would be possible at higher grid resolution where reconnecting current sheets become unstable to tearing (Ripperda et al. 2021).

In this work, we have used the free parameter $\mathcal{C}_{\min}$ to address the systematic uncertainty in the energetics of reconnecting current sheets in ideal GRMHD. High values of $\mathcal{C}_{\min}$ mimic a relatively low resistivity with thinner, longer and less numerous current sheets while low values of $\mathcal{C}_{\min}$ mimic a higher resistivity with larger, longer and more numerous current sheets. This method is not self-consistent, since our choice of $\mathcal{C}_{\min}$ does not influence the dynamics of the plasma. We consider it a step towards incorporating the results of kinetic reconnection studies into GRMHD simulations (see also e.g. Ball et al. 2018; Chatterjee et al. 2020). We have shown that $\mathcal{C}_{\min}$ mainly acts as a normalization factor for the X-ray intensity during the flares. We find that good agreement with the observed Sgr A∗ X-ray luminosity in both flares and quiescence, as well as the spectral index, is possible for a value of $\mathcal{C}_{\min} \approx 1$, which is consistent with a current sheet of thickness the size of a cell at our resolution. Even a relatively modest rate of non-thermal electron acceleration in current sheets can produce the X-ray emission needed to explain the flares of Sgr A∗. The very low level of the quiescent X-rays provides a strong constraint on the steady rate of energy injection.

We have also neglected relativistic effects in calculating the resulting spectra. Fig. 7 compares NIR light curves calculated by our method (incorporating non-thermal as well as thermal electrons) to those calculated using fully relativistic radiative transfer but only including thermal electrons (Dexter et al. 2020b). Similar flaring

behaviour and median luminosity are seen in both cases, with order-unity errors, although the flaring NIR emission comes from very close to the black hole. Another approximation was to neglect Compton scattering. However, we find that in our model $U_B/U_{ph} > 100$ where $U_{ph} \simeq L_{bol}/(4\pi r_{out}^2 c)$, with L_{bol} the bolometric luminosity from our model with $\mathcal{C}_{min} = 5$ and $r_{out} = 30\,r_g$, and $U_B \simeq B_{mean}^2$ with B_{mean}^2 being the magnetic energy density averaged over a sphere of radius r_{out}. This suggests that synchrotron emission is dominant over Compton scattering and justifies our approximation. Finally, to estimate the impacts of cooling on the accelerated electrons, we compared the synchrotron cooling time-scale with the light crossing time-scale. Obtaining a more accurate form for the distribution function would require following the histories of high-energy particles injected locally in a current sheet. Particles could leave the system very rapidly before they can efficiently cool down, or get trapped in the turbulent disc and get accelerated by diffusive processes while cooling at the same time. By following the evolution of test (tracer) particles in GRMHD simulations, such calculations should become possible in the near future.

ACKNOWLEDGEMENTS

DATA AVAILABILITY

The simulation data analyzed in this article will be shared on reasonable request to the corresponding author.

REFERENCES

Baganoff F. K. et al., 2001, Nature, 413, 45
Baganoff F. K. et al., 2003, ApJ, 591, 891
Balbus S. A., Hawley J. F., 1991, ApJ, 376, 214
Balbus S. A., Hawley J. F., 1998, Rev. Mod. Phys., 70, 1
Balick B., Brown R. L., 1974, ApJ, 194, 265
Ball D., Özel F., Psaltis D., Chan C.-k., 2016, ApJ, 826, 77
Ball D., Sironi L., Özel F., 2018, ApJ, 862, 80
Bessho N., Bhattacharjee A., 2012, ApJ, 750, 129
Bisnovatyi-Kogan G., Ruzmaikin A., 1974, Astrophys. Space Sci., 28, 45
Blumenthal G. R., Gould R. J., 1970, Rev. Mod. Phys., 42, 237
Bodo G., Tavecchio F., Sironi L., 2021, MNRAS, 501, 2836
Bower G. C. et al., 2019, ApJ, 881, L2
Cerutti B., Werner G. R., Uzdensky D. A., Begelman M. C., 2012, ApJ, 754, L33
Cerutti B., Werner G. R., Uzdensky D. A., Begelman M. C., 2013, ApJ, 770, 147
Chael A., Rowan M., Narayan R., Johnson M., Sironi L., 2018, MNRAS, 478, 5209
Chan C.-k., Psaltis D., Özel F., Medeiros L., Marrone D., Sadowski A., Narayan R., 2015a, ApJ, 812, 103
Chan C.-k., Psaltis D., Özel F., Narayan R., Sadowski A., 2015b, ApJ, 799, 1
Chatterjee K. et al., 2021, MNRAS, 507, 5281
Connors R. M. T. et al., 2017, MNRAS, 466, 4121
Dexter J., Fragile P. C., 2013, MNRAS, 432, 2252
Dexter J., Agol E., Fragile P. C., 2009, ApJ, 703, L142
Dexter J., Agol E., Fragile P. C., McKinney J. C., 2010, ApJ, 717, 1092
Dexter J. et al., 2020a, MNRAS, 494, 4168
Dexter J. et al., 2020b, MNRAS, 497, 4999
Dibi S., Drappeau S., Fragile P. C., Markoff S., Dexter J., 2012, MNRAS, 426, 1928
Dibi S., Markoff S., Belmont R., Malzac J., Neilsen J., Witzel G., 2016, MNRAS, 461, 552
Do T. et al., 2019, ApJ, 882, L27
Dodds-Eden K. et al., 2009, ApJ, 698, 676
Doeleman S. S. et al., 2008, Nature, 455, 78
Eckart A. et al., 2006a, A&A, 450, 535
Eckart A., Schödel R., Meyer L., Trippe S., Ott T., Genzel R., 2006b, A&A, 455, 1
Eckart A. et al., 2012, A&A, 537, A52
Fishbone L. G., Moncrief V., 1976, ApJ, 207, 962
Gammie C. F., McKinney J. C., Tóth G., 2003, ApJ, 589, 444
Genzel R., Schödel R., Ott T., Eckart A., Alexander T., Lacombe F., Rouan D., Aschenbach B., 2003, Nature, 425, 934
Ghez A. M., Salim S., Hornstein S. D., Tanner A., Lu J. R., Morris M., Becklin E. E., Duchêne G., 2005, ApJ, 620, 744
Gillessen S. et al., 2017, ApJ, 837, 30
Gravity Collaboration, 2018a, A&A, 615, L15
Gravity Collaboration, 2018b, A&A, 618, L10
Gravity Collaboration, 2020a, A&A, 635, A143
Gravity Collaboration, 2020b, A&A, 638, A2
Gravity Collaboration, 2020c, A&A, 643, A56
Guo F., Li H., Daughton W., Liu Y.-H., 2014, Phys. Rev. Lett., 113, 155005
Guo F. et al., 2016, ApJ, 818, L9
Haggard D. et al., 2019, ApJ, 886, 96
Hakobyan H., Petropoulou M., Spitkovsky A., Sironi L., 2021, ApJ, 912, 48
Hirose S., Krolik J. H., De Villiers J.-P., Hawley J. F., 2004, ApJ, 606, 1083
Howes G. G., 2010, MNRAS, 409, L104
Igumenshchev I. V., 2008, ApJ, 677, 317
Kagan D., Milosavljević M., Spitkovsky A., 2013, ApJ, 774, 41
Kawazura Y., Barnes M., Schekochihin A. A., 2019, Proc. Natl. Acad. Sci., 116, 771
Markoff S., Falcke H., Yuan F., Biermann P. L., 2001, A&A, 379, L13
Marrone D. P. et al., 2008, ApJ, 682, 373
Mayer-Hasselwander H. et al., 1998, A&A, 335, 161
Mościbrodzka M., Gammie C. F., Dolence J. C., Shiokawa H., Leung P. K., 2009, ApJ, 706, 497
Neilsen J. et al., 2013, ApJ, 774, 42
Neilsen J. et al., 2015, ApJ, 799, 199
Nowak M. A. et al., 2012, ApJ, 759, 95
Pandya A., Zhang Z., Chandra M., Gammie C. F., 2016, ApJ, 822, 34
Petersen E., Gammie C., 2020, MNRAS, 494, 5923
Petropoulou M., Sironi L., 2018, MNRAS, 481, 5687
Ponti G. et al., 2017, MNRAS, 468, 2447
Porth O., Mizuno Y., Younsi Z., Fromm C. M., 2021, MNRAS, 502, 2023
Quataert E., 2002, ApJ, 575, 855
Ressler S. M., Tchekhovskoy A., Quataert E., Chandra M., Gammie C. F., 2015, MNRAS, 454, 1848
Ressler S. M., Tchekhovskoy A., Quataert E., Gammie C. F., 2017, MNRAS, 467, 3604
Ripperda B., Bacchini F., Philippov A. A., 2020, ApJ, 900, 100
Ripperda B., Liska M., Chatterjee K., Musoke G., Philippov A. A., Markoff S. B., Tchekhovskoy A., Younsi Z., 2021, ApJL, 924, L32
Rowan M. E., Sironi L., Narayan R., 2017, ApJ, 850, 29
Ryan B. R., Ressler S. M., Dolence J. C., Tchekhovskoy A., Gammie C., Quataert E., 2017, ApJ, 844, L24
Schödel R., Morris M. R., Muzic K., Alberdi A., Meyer L., Eckart A., Gezari D. Y., 2011, A&A, 532, A83
Shcherbakov R. V., Penna R. F., McKinney J. C., 2012, ApJ, 755, 133
Sironi L., Spitkovsky A., 2014, ApJ, 783, L21
Tchekhovskoy A., 2019, HARMPI: 3D Massively Parallel General Relativictic MHD Code, preprint (ascl:1912.014), Astrophysics Source Code Library

Tchekhovskoy A., Narayan R., McKinney J. C., 2011, MNRAS, 418, L79
Uzdensky D. A., Cerutti B., Begelman M. C., 2011, ApJ, 737, L40
Viergutz S. U., 1993, A&A, 272, 355
Werner G. R., Uzdensky D. A., Cerutti B., Nalewajko K., Begelman M. C., 2016, ApJ, 816, L8
Werner G. R., Uzdensky D. A., Begelman M. C., Cerutti B., Nalewajko K., 2018, MNRAS, 473, 4840
Werner G. R., Philippov A. A., Uzdensky D. A., 2019, MNRAS, 482, L60

White C. J., Quataert E., 2021, preprint (arXiv:2104.12896)
Yuan F., Narayan R., 2014, ARA&A, 52, 529
Yusef-Zadeh F., Wardle M., Heinke C., Dowell C. D., Roberts D., Baganoff F. K., Cotton W., 2008, ApJ, 682, 361
Zhdankin V., Uzdensky D. A., Perez J. C., Boldyrev S., 2013, ApJ, 771, 124

This paper has been typeset from a TeX/LaTeX file prepared by the author.